

Effective dispersion and separation resolution in continuous particle fractionation

Stefano Cerbelli¹ · Fabio Garofalo^{1,2} · Massimiliano Giona¹

Received: 15 January 2015 / Accepted: 25 June 2015 / Published online: 9 August 2015
© Springer-Verlag Berlin Heidelberg 2015

Abstract Theoretical models and experiments suggest that the transport of suspended particles in microfluidics-based sorting devices can be modeled by a two-dimensional effective advection-diffusion process characterized by constant average velocity, \mathbf{W} , and a typically anisotropic dispersion tensor, \mathbb{D} , whose principal axes are slanted with respect to the direction of the effective velocity. We derive a closed-form expression connecting the effective transport parameters to separation resolution in continuous particle fractionation. We show that the variance of the steady-state particle concentration profile at an arbitrary cross-section of the device depends upon a scalar dispersion parameter, D_{eff} , which is primarily controlled by the projection of the dispersion tensor onto the direction orthogonal to \mathbf{W} . Numerical simulations of particle transport in a Deterministic Lateral Displacement device, here used as a benchmark to illustrate the practical use of the effective transport approach, indicate that sustained dispersion regimes typically arise, where the dispersion parameter D_{eff} can be orders of magnitude larger than the bare particle diffusivity.

Keywords Fractionation · Dispersion · Resolution · Effective transport · Periodic media

List of symbols

Latin symbols

- $C(\xi_1, \xi_2, t)$ Effective particle number density function in the $\xi_1\xi_2$ frame (see Fig. 8)
 $C_\infty(\xi_1, \xi_2)$ Steady-state effective particle number density in the $\xi_1\xi_2$ frame
 D_α, \mathcal{D} Diffusion coefficient of species α
 D_{eff} Dispersion coefficient for the continuous separation process

Coordinate system

- D_1, D_2 Dimensionless dispersion coefficients (principal values of \mathbb{D})
 $\text{Pe} = U\ell/\mathcal{D}$ Particle Peclet number
 $R(\bar{x})$ Resolution of a binary mixture at downstream distance \bar{x} from the inlet
 $Y(\bar{x})$ Average y crossing coordinate at an exit section at downstream distance \bar{x} from the inlet
 \mathbf{W}_α Average (vector) velocity of species α
 W_{ξ_i} Components of \mathbf{W} in the $\xi_1\xi_2$ coordinate system

Greek symbols

- $\Phi_\alpha(x, y, t)$ Effective particle concentration n in the global coordinate system xy
 $\Phi_\infty(x, y)$ Steady-state effective particle concentration in the global coordinate system xy
 $\Phi_\nu(\bar{x}, y)$ Normalized cross-sectional steady-state distribution of particle crossing coordinate at downstream distance \bar{x} from the inlet
 $\sigma(\bar{x}, y)$ Variance of $\Phi_\nu(\bar{x}, y)$ profile
 $\Theta_{\mathbb{D}}$ Angle between the eigendirection $\mathbf{e}_{\mathbb{D}}^{(1)}$ of \mathbb{D} and the average velocity of the carrier flow (see Fig. 1b)

✉ Stefano Cerbelli
stefano.cerbelli@uniroma1.it

¹ Dipartimento di Ingegneria Chimica Materiali Ambiente, Sapienza Università di Roma, IT, Rome, Italy

² Present Address: Department of Biomedical Engineering, Lund University, Ole Römers Väg 3, 22363 Lund, Sweden

Θ'_w Angle between the eigendirection $\mathbf{e}_D^{(1)}$ of \mathbb{D} and the average particle velocity (see Fig. 1b)

Calligraphic and miscellaneous symbols

\mathbb{D} Effective dispersion tensor

1 Introduction

In the last two decades, the family of microfluidics-based prototypes devised for sorting mixtures of mesoscopic objects suspended in a buffer fluid has been continuously increasing. While most of the processes carried out in these devices are dissimilar by the nature of the suspended objects [ranging from healthy and tumoral cells Autebert et al. (2012) to DNA fragments Dorfman et al. (2013), Raynal et al. (2013), Benke et al. (2013), and encompassing viruses and proteins Sia and Whitesides (2003)], by the feature driving the separation [e.g. size Huang et al. (2004), electric surface charge Dorfman et al. (2013), permanent or induced dipole Zhang et al. (2010), dielectric constant Jonas and Zemanek (2008), acoustic contrast factor Bruus (2012)], as well as by the operating conditions (transient or continuous), they all share a common governing transport mechanism, namely the micro-dynamical interaction between a deterministic drive (be it Stokesian drag, electric field, magnetic field, laser light, or acoustic pressure) and Brownian fluctuations. Because of the micrometric or sub-micrometric size of the suspended objects, the effect of stochastic fluctuations cannot be overlooked in any physically realistic model of transport. With the exception of few specific applications [e.g. Brownian ratchets Hnggi and Marchesoni (2009), Huang et al. (2003)], where the different level of fluctuation intensities can be regarded as the ultimate source for the separation, the presence of diffusion generally hinders separation with respect to what can be predicted on the basis of a purely deterministic transport model. Furthermore, there are reasons to believe

that the negative impact of Brownian motion on separation performance may go well beyond what could be anticipated from the value of the bare particle diffusivity, since dispersion-enhanced regimes might arise, which can be regarded as the large-scale outcome of the synergistic interaction between the small-scale structure of the deterministic drive and the stochastic fluctuations.

One of the arguments that supports this idea is that such dispersion-enhanced regimes have been known to occur when the suspended objects can be assimilated to massless tracers and when the deterministic drive is represented by an incompressible flow, which can be regarded as stemming from a vector potential. In this case, a complete understanding of large-scale transport has been achieved in a variety of flows, from the classical closed-form expression of the effective axial dispersion coefficient in Taylor-Aris treatment of duct flows, to Brenner's macrotransport paradigm for incompressible spatially-periodic flows, where enhanced-dispersion regimes have been analyzed and quantified in various lattice geometries [see Ref. Brenner and Edwards (1993) and therein cited references]. On the one hand, these theories cannot be directly implemented to particle sorting processes since the very source of separation is here typically represented by a scalar potential, a condition that makes the vector field representing the deterministic drive not altogether incompressible. On the other hand, increasing numerical evidence is becoming available Ghosh et al. (2012), Speer et al. (2012), Cerbelli et al. (2013), Cerbelli (2013), Chen (2013), Kirchner and Hasselbrink (2005), suggesting that even in the presence of mixed potentials (i.e. possessing both scalar and vector components), particle transport is consistent with an effective template which can be regarded as a generalization of the behavior of point tracers entrained in incompressible flows. Just like the incompressible case, this template is characterized by a constant effective velocity and a—typically anisotropic—constant effective dispersion tensor, whose principal axes are slanted with respect to the effective particle velocity as well as to the average direction of

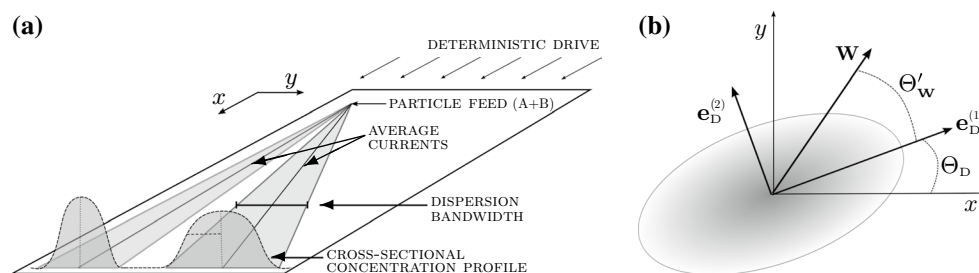


Fig. 1 **a** Schematic representation of continuous fractionation for a binary mixture of particles. The average, large-scale component of the deterministic drive is assumed aligned with the x -axis. **b** Geometric parameters defining the effective transport model. The shaded

area represents the dispersion ellipsoid, $\mathbf{e}_D^{(1)}$, $\mathbf{e}_D^{(2)}$ its eigenvectors corresponding to the eigenvalues D_1 , D_2 , \mathbf{W} is the large-scale average particle velocity

the deterministic drive. The main difference induced by the presence of the dissipative scalar potential is that here the effective particle velocity needs not be aligned with the average direction of the deterministic drive. Indeed, it is this very effect that acts as a driving force for the separation in that the structure of the scalar potential is specific to the particle feature, such as size, shape, charge, dipole, etc., so that particles possessing different characteristics experience different dissipative potentials and therefore migrate along different directions. Besides, the dispersion-enhancing effect of the deterministic drive quantitatively translates into the fact that some of the entries of the effective dispersion tensor can be orders of magnitude larger than the bare particle diffusivity. This effect must be clearly characterized and predicted at the design stage of the process if one is to avoid unchecked negative effects on separation resolution. Notwithstanding the possible occurrence of convection-enhanced dispersion, the design of most microfluidic separators is still largely based on a purely deterministic (diffusionless) setting Huang et al. (2004), Inglis et al. (2006), Kralj et al. (2006), Inglis (2009), Louterback et al. (2010), Frechette and Drazer (2009), Long et al. (2008), and the theoretical effort put forward to quantify the impact of particle diffusion on the deterministic transport has been mainly limited to predict the effect of Brownian noise on the average particle velocity Gleeson et al. (2006), Heller and Bruus (2008), thus overlooking dispersion phenomena about the average particle current.

Alongside these numerical studies, a number of recent experiments showed how particle dispersion and separation resolution can be quite sensitive to the process conditions, particle size, and device geometry Collins et al. (2014), Devendra and Drazer (2012), He et al. (2013, 2014), Bogunovic et al. (2012), Inglis et al. (2008), Jain and Posner (2008), Huang et al. (2004), sometimes with a counter-intuitive dependence. This is the case, for instance, of the gravity-driven Deterministic Lateral Displacement separation experiments reported in Ref. Devendra and Drazer (2012), which show unambiguously how particle dispersion can increase when increasing particle size (i.e. at increasing particle Peclet number). These results suggest that a consistent interpretation of experiments and a rational design of microfluidics-assisted particle sorters cannot do away with a tailored modelling of effective transport. The aim of this article is to provide a quantitative framework to bridge the gap between theoretical modelling and experiments. We focus specifically on continuous separation processes, which are attracting increasing interest in separation science in view of their operational simplicity, high throughput, and integrability with Lab-on-Chip technology Han and Frazier (2008), Kulrattanarak et al. (2008), Lenshof and Laurell (2010), Ling et al. (2012). The article is divided into two main parts, the first developing the steady-state solution for the particle number density associated with

a given generic set of effective transport parameters, the second providing a concrete example of how these parameters depend on the device geometry and particle features in a typical fractionation process.

2 Steady-state particle concentration from a continuous localized source

In what follows, we consider a generic setting of a continuous fractionation process such as that schematically illustrated in Fig. 1a. A localized stream of buffer fluid entraining two species of suspended particles, labeled “A” and “B”, is continuously fed at a point of the separation device, which is henceforth assumed as the origin of the global Cartesian reference frame $x - y$. Because of their different nature (e.g. size, electric charge, etc.), the particles react specifically to the deterministic drive, so that the continuous feed stream splits into two currents, each characterized by an average deflection angle, say θ_A and θ_B , respectively. Also, owing to the presence of Brownian fluctuations, quantified by the bulk particle diffusivities \mathcal{D}_A and \mathcal{D}_B , dispersion of individual particle paths about the average current should be expected, resulting in a dispersion bandwidth that increases as one proceeds downstream the average current. If a two-dimensional effective transport template can be enforced to describe the motion of each particle species, the evolution of the particle number density function, $\Phi_\alpha(x, y, t)$ (henceforth referred to as *effective particle concentration*), is governed by the macrotransport advection-diffusion equation

$$\partial_t \Phi_\alpha = -\mathbf{W}_\alpha \cdot \nabla \Phi_\alpha + \nabla \cdot (\mathbb{D}_\alpha \cdot \nabla \Phi_\alpha) + F_\alpha \delta(\mathbf{x}), \quad (1)$$

where $\alpha = \text{“A”}, \text{“B”}$, \mathbf{W}_α and $\mathbb{D}_\alpha = ((D_{\alpha,ij}))$ represent the particle effective velocity and the effective dispersion tensor, respectively, F_α the number of α -particles released in the unit time in the transport domain, and $\delta(\mathbf{x})$ is the Dirac’s delta function representing a feed stream localized at the origin of the coordinate system. As we consider separately the transport of each particle species, we henceforth drop the subscript “ α ”.

It can be observed that both the effective velocity, \mathbf{W} , and the dispersion tensor \mathbb{D} depend—in a markedly non-trivial fashion—upon the interaction between the deterministic drive, often possessing a small-scale spatially fluctuating component Devendra and Drazer (2012), MacDonald et al. (2003), and the isotropic bulk diffusion experienced by the particles. A detailed explanation of such dependence is the object of current research in microfluidic-assisted separations and will be addressed in a later section of this article, where a recently proposed model Cerbelli et al. (2013) of size-based separation in deterministic lateral displacement devices is used to illustrate potentialities and limitations

of the effective transport approach. For the time being, we just *assume* that the effective transport model in Eq. (1) holds true in order to derive the relationship between the effective parameters \mathbf{W} , \mathbb{D} , and the steady-state dispersion bandwidth about the average current depicted in Fig. 1a. Note that by the symmetry of the effective dispersion tensor, the transport parameters amount to five independent scalar quantities, which we next identify as the magnitude $W = \|\mathbf{W}\|$ of the effective velocity, the principal (eigen-) values $\widetilde{D}_1, \widetilde{D}_2$ of \mathbb{D} , the angle Θ_D between the eigenvector $\mathbf{e}_D^{(1)}$ associated with \widetilde{D}_1 and the x -axis, and the angle Θ'_W between the effective velocity and $\mathbf{e}_D^{(1)}$ (see Fig. 1b).

Next, we proceed to derive the solution $C(\xi_1, \xi_2, t) = \Phi(x, y, t)$ to Eq. (1) by using a new Cartesian coordinate system $\xi_1 \xi_2$, still centered at the origin of the $x - y$ system, whose axes are collinear with the eigenvectors $\mathbf{e}_D^{(1)}$ and $\mathbf{e}_D^{(2)}$ of the dispersion tensor, respectively. Also, we assume that Eq. (1) has been made dimensionless by assuming a characteristic length ℓ , the characteristic velocity W , the characteristic time ℓ/W , and the reference concentration $F\ell/W$, so that, in the chosen frame, the dimensionless velocity is given by $\mathbf{W} = (\cos \Theta'_W, \sin \Theta'_W)$, and the dimensionless dispersion tensor by $\mathbb{D} = \text{diag}(D_1, D_2) = \text{diag}(\widetilde{D}_1/(U\ell), \widetilde{D}_2/(U\ell))$, where D_1 and D_2 are the dimensionless dispersion coefficients. In this setting, Eq. (1) can be rewritten as

$$\frac{\partial C}{\partial t} = -W_{\xi_1} \frac{\partial C}{\partial \xi_1} - W_{\xi_2} \frac{\partial C}{\partial \xi_2} + D_1 \frac{\partial^2 C}{\partial \xi_1^2} + D_2 \frac{\partial^2 C}{\partial \xi_2^2} + \delta(\xi_1, \xi_2), \quad (2)$$

where $W_{\xi_1} = \cos(\Theta'_W)$, $W_{\xi_2} = \sin(\Theta'_W)$. This equation is equipped with the initial condition $C(\xi_1, \xi_2, 0) = 0$, expressing the fact that the transport domain is devoid of particles at the beginning of the transport process. The Green function, $\mathcal{G}(\xi_1, \xi_2, t)$, for this problem is given by

$$\mathcal{G}(\xi_1, \xi_2, t) = \frac{1}{4\pi\sqrt{D_1 D_2} t} \exp\left\{-\frac{(\xi_1 - W_{\xi_1} t)^2}{4D_1 t} - \frac{(\xi_2 - W_{\xi_2} t)^2}{4D_2 t}\right\} \quad (3)$$

The solution at time t can therefore be expressed as

$$C(\xi_1, \xi_2, t) = \int_0^t \mathcal{G}(\xi_1, \xi_2, \tau) d\tau \quad (4)$$

in that by the linearity of the transport process, each elementary mass released between τ and $\tau + d\tau$ evolves independently of past and future events, and therefore the contribution to the current concentration field is simply the superposition of all of the elementary dispersion events for $0 < \tau \leq t$. The steady-state field $C_\infty(\xi_2, \xi_2)$ is therefore given by the time-asymptotic limit of Eq. (4),

$$C_\infty(\xi_1, \xi_2) = \int_0^\infty \mathcal{G}(\xi_1, \xi_2, t) dt. \quad (5)$$

By setting

$$\begin{aligned} A &= \left(1/(4\pi\sqrt{D_1 D_2})\right) \\ \alpha(\xi_1, \xi_2) &= \xi_1^2/(4D_1) + \xi_2^2/(4D_2) \\ \beta(\xi_1, \xi_2) &= W_{\xi_1}\xi_1/(2D_1) + W_{\xi_2}\xi_2/(2D_2) \\ \Gamma &= W_{\xi_1}^2/(4D_1) + W_{\xi_2}^2/(4D_2) \end{aligned} \quad (6)$$

the integral at the r.h.s. of Eq. (5) becomes

$$C_\infty(\xi_1, \xi_2) = A \exp[\beta(\xi_1, \xi_2)] \times \int_0^\infty \frac{1}{t} \exp\left[-\left(\frac{\alpha(\xi_1, \xi_2)}{t} + \Gamma t\right)\right] dt \quad (7)$$

By setting $s = \Gamma t$, the r.h.s. of Eq. (7) can be written as

$$C_\infty(\xi_1, \xi_2) = A \exp[\beta(\xi_1, \xi_2)] \times \int_0^\infty \frac{1}{s} \exp\left[-\left(s + \frac{\Gamma\alpha(\xi_1, \xi_2)}{s}\right)\right] ds \quad (8)$$

This integral is of the form

$$\int_0^\infty x^{\nu-1} \exp\left[-\left(x + \frac{\mu^2}{4x}\right)\right] = 2\left(\frac{\mu}{2}\right)^\nu K_\nu(x) \quad (9)$$

and can be computed in closed-form [see, e.g., ef. Gradshteyn and Ryzhik (2007)] ultimately yielding

$$C_\infty(\xi_1, \xi_2) = 2A \exp\{\beta(\xi_1, \xi_2)\} K_0\left(2\sqrt{\Gamma\alpha(\xi_1, \xi_2)}\right) \quad (10)$$

where $K_0(\eta)$ denotes the modified Bessel function of the second kind Polyanin and Manzhirov (2007). Once this solution is known, the steady state Φ_∞ field in the xy coordinate system can be obtained as $\Phi_\infty(x, y) = C_\infty(\xi_1(x, y), \xi_2(x, y))$, where $\begin{pmatrix} \xi_1(x, y) \\ \xi_2(x, y) \end{pmatrix} = \begin{pmatrix} \cos \Theta_D & \sin \Theta_D \\ -\sin \Theta_D & \cos \Theta_D \end{pmatrix} \cdot \begin{pmatrix} x \\ y \end{pmatrix}$.

In prototypical experiments using long-exposure micrograph Huang et al. (2004), fluorescence intensity of marked particles is typically measured along a cross-section of the device, at a distance \bar{x} from the feed source. At steady-state, this profile is clearly proportional to the normalized profile

$$\Phi_\nu(\bar{x}, y) = \frac{\Phi_\infty(\bar{x}, y)}{\int_{-\infty}^\infty \Phi_\infty(\bar{x}, y) dy} \quad (11)$$

The average y -coordinate, $Y(\bar{x})$, of particles paths crossing the device section at $x = \bar{x}$, and the squared variance $\sigma^2(\bar{x})$ of the actual crossing ordinate about the average value, are thus given by

$$\begin{aligned} Y(\bar{x}) &= \int_{-\infty}^\infty y \Phi_\nu(\bar{x}, y) dy \\ \sigma^2(\bar{x}) &= \int_{-\infty}^\infty (y - Y(\bar{x}))^2 \Phi_\nu(\bar{x}, y) dy \end{aligned} \quad (12)$$

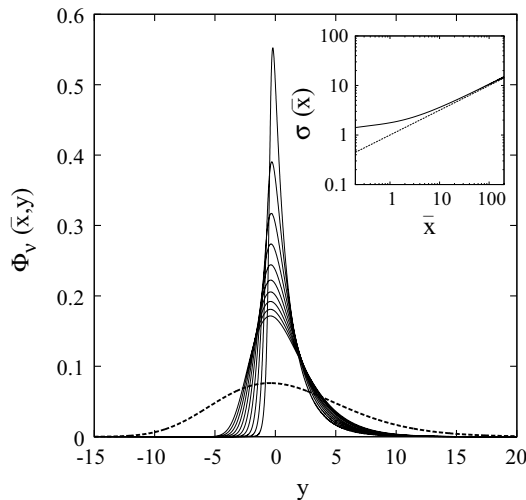


Fig. 2 *Main panel:* Normalized particle concentration profiles near (*continuous lines*, $0 < \bar{x} \leq 4$) and far from the particle feed source (*broken line*, $\bar{x} = 25$). The concentration profiles in the direction orthogonal to \mathbf{W} attain a Gaussian-like structure when moving downstream the effective velocity direction. Inset: $\sigma(\bar{x})$ versus \bar{x} (*continuous line*). The *broken line* depicts the scaling $\sigma(\bar{x}) \simeq \sqrt{2D_{\text{eff}} \bar{x}}$

On the assumption that the normalized concentration profile $\Phi_v(\bar{x}, y)$ be symmetric with respect to the average $Y(\bar{x})$, these quantities are the primary parameters controlling separation resolution. For instance, in the case of a binary separation of “A” and “B” particle types, the resolution $R(\bar{x})$ at \bar{x} can be defined as Giddings (1991)

$$R(\bar{x}) = \frac{|Y_A(\bar{x}) - Y_B(\bar{x})|}{2(\sigma_A(\bar{x}) + \sigma_B(\bar{x}))}. \tag{13}$$

If the averages and variances are known as functions of the cross-section position \bar{x} , then the minimum device length for accomplishing the separation can be computed by requiring that $R(\bar{x})$ be equal to a prescribed target value.

To illustrate the effect on anisotropic diffusivity on the steady-state particle distribution, Fig. 2 depicts the structure of the cross-sectional normalized profiles for the case where the average velocity \mathbf{W} is parallel to the x -axis, $\Theta_D = \pi/4$, and the dimensionless diffusivities are given by $D_1 = 0.1$, and $D_2 = 1$.

As can be observed, the near-field profiles (*continuous lines*) possess strongly asymmetric structure, an asymmetry which is progressively lost at larger distances from the particle feed, where the profile attains an almost Gaussian-like structure, as depicted by the broken line representing $\Phi_v(\bar{x}, y)$ at $\bar{x} = 25$. The inset in the figure shows the increase of the profile variance as one moves downstream the effective velocity direction, here parallel to the x -axis. After a brief spatial transient, the variance approaches the scaling

$$\sigma(\bar{x}) \simeq \sqrt{2D_{\text{eff}} \bar{x}}, \tag{14}$$

where D_{eff} can be regarded as a phenomenological coefficient, henceforth referred to as *continuous dispersion coefficient*, that is specific to continuous separation processes. In the next section we investigate how D_{eff} depends upon the dimensionless parameters D_1, D_2, Θ_D , and Θ'_W .

3 Continuous dispersion coefficient from macrotransport parameters

In principle, the analytical expression in Eq. (10) provides all of the information useful to characterize the entire normalized profiles, including its average and variance defined by Eq. (12) (or any higher order moment, for that matter). However, in the actual computation of $C_\infty(\xi_1, \xi_2)$, one faces the problem that in practical applications the function $\beta(\xi_1, \xi_2)$, and the product $2\sqrt{\Gamma\alpha(\xi_1, \xi_2)}$ defined by Eq. (6) typically attain very large values (e.g. of order 10^3), so that the C_∞ field defined by Eq. (10) results as the product of an exponential function rapidly diverging to $+\infty$ times a factor (the Bessel function) quickly decaying to zero. This makes a direct approach to the determination of the steady-state profile practically unfeasible, even though a closed-form solution is available. An efficient way to bypass this representation problem is to consider the asymptotic approximation to the modified Bessel function $K_0(\eta)$ at large values of its argument, which yields Abramowitz and Stegun (1972)

$$K_0(\eta) \simeq e^{-\eta} \sqrt{\pi/(2\eta)} \quad \text{as } \eta \rightarrow \infty. \tag{15}$$

This implies that whenever $2\sqrt{\Gamma\beta(\xi_1, \xi_2)}$ is sufficiently large (which, in turn, implies $\xi_1^2 + \xi_2^2 \rightarrow \infty$), the steady-state field can be approximated as

$$\begin{aligned} C_\infty(\xi_1, \xi_2) &\simeq \frac{A}{\sqrt{\pi}} \frac{\exp\{\beta(\xi_1, \xi_2) - 2\sqrt{\Gamma\beta(\xi_1, \xi_2)}\}}{\sqrt[4]{\Gamma\beta(\xi_1, \xi_2)}} \\ &= \frac{A}{\sqrt{\pi}} \frac{\exp\{\beta(\xi_1, \xi_2) - h(\xi_1, \xi_2)\}}{\sqrt{h(\xi_1, \xi_2)}}, \end{aligned} \tag{16}$$

where $h(\xi_1, \xi_2) = 2\sqrt{\Gamma\beta(\xi_1, \xi_2)}$. This approximate solution lends itself to a handier analysis, which we carry out in the coordinate system $\xi_1\xi_2$ for simplicity of notation. First, we observe that upon the straight line r through the origin parallel to \mathbf{W} , i.e. with parametric representation ($\xi_1 = \cos\Theta'_W s, \xi_2 = \sin\Theta'_W s$) where s is the arc length on r from the origin, the argument of the exponential function in Eq. (16) vanishes together with its first derivatives (see “Appendix”). The estimate of the continuous dispersion coefficient from the effective transport parameters can thus be obtained by expanding along the y direction the approximate field in Eq. (16) in Taylor series about the point $(\bar{x}, \tan(\Theta_D + \Theta'_W)\bar{x})$ lying at the intersection between r and the device cross-section at \bar{x} . In this expansion, the denominator at the r.h.s. of Eq. (16) is assumed

slowly varying in all of the points where the numerator is significantly different from zero. One shows that, within this approximation (see “Appendix”),

$$D_{\text{eff}} = \frac{D_1 \sin^2 \Theta'_W + D_2 \cos^2 \Theta'_W}{|\cos^3(\Theta'_W + \Theta_D)|} = \frac{D_{\perp}}{|\cos^3 \Theta_W|}, \quad (17)$$

where $D_1 \sin^2 \Theta'_W + D_2 \cos^2 \Theta'_W = D_{\perp}$, and where $\Theta_W = \Theta'_W + \Theta_D$ is the angle between \mathbf{W} and the x axis (see Fig. 1b). Equation (17) constitutes the relationship sought between the dispersion coefficient under steady-state conditions and the effective transport parameters. It is readily seen that D_{\perp} represents the projection of the dispersion tensor onto the direction orthogonal to \mathbf{W} , i. e. $D_{\perp} = \mathbf{n}_W \cdot \mathbb{D} \cdot \mathbf{n}_W$, where \mathbf{n}_W is a unit vector orthogonal to \mathbf{W} . The denominator of the same relationship yields a correction factor which accounts for the fact that the average particle stream is slanted with respect to the cross-section, here assumed orthogonal to the x axis of the global coordinate system.

A yet deeper understanding of continuous dispersion can be gained by considering the process in an orthogonal reference frame $\eta_1 \eta_2$, still centered at the feed source point, where one of the axis, say η_1 , is collinear with the r line above defined (i.e. is parallel to the effective velocity \mathbf{W}). Because the argument of the exponential in Eq. (16) vanishes identically on r , the solution onto this particular line attains the form

$$C_{\infty}(\xi_1(\eta_1), \xi_2(\eta_1)) = \frac{1}{\sqrt{2\pi D_{\parallel}} \eta_1} \quad (\eta_2 = 0) \quad (18)$$

where

$$D_{\parallel} = D_1 \cos^2 \Theta'_W + D_2 \sin^2 \Theta'_W \quad (19)$$

is the projection of the dispersion tensor onto the direction parallel to \mathbf{W} , i.e. $D_{\parallel} = \mathbf{t}_W \cdot \mathbb{D} \cdot \mathbf{t}_W$, \mathbf{t}_W being a unit vector parallel to \mathbf{W} . From the above observations, one gathers that the steady-state dispersion process from a continuous localized source depends upon the *two coefficients*, D_{\parallel} and D_{\perp} , the first controlling the rate of decay of the peak intensity along the average particle current, the second quantifying the growth of the variance associated with the normalized one-dimensional concentration profile taken along the direction orthogonal to the effective particle velocity. In turn, this implies that one could infer on the anisotropic character of the effective dispersion tensor by steady-state measures of fluorescence intensity along two orthogonal directions, one of which is collinear with the average particle current. It is almost superfluous to remark how such steady-state measurements are much easier to obtain experimentally since long-time exposure detection can be used, which bypasses

the sensitivity limits associated with instantaneous fluorescence measures.

4 Case study

As discussed above, there are many physical contexts where the interaction between a deterministic drive and isotropic Brownian motion at small spatial scales gives rise to complex transport regimes characterized by an anisotropic large-scale dispersion process Gross et al. (2014). In microfluidic processes devised to separate suspended objects, the small scale is usually provided by the smallest characteristic length of variation of the deterministic drive, whose structure often possesses a spatially periodic two-dimensional component. This is the case, e.g. of optical lattices MacDonald et al. (2003), or solid impermeable obstacle arrays Louterback et al. (2009), Devendra and Drazer (2012), Green et al. (2009), Huang et al. (2004). In this section, we use the latter example, usually referred to as Deterministic Lateral Displacement (henceforth DLD), as a benchmark to show the occurrence of dispersion-enhanced regimes in continuous fractionation processes. The core of separation devices exploiting this size-based sorting principle is a shallow rectangular channel which hosts a two-dimensional spatially periodic lattice of identical micrometer-sized obstacles, typically of cylindrical shape (see Fig. 3a).

The lattice is slanted by an angle Θ_l with respect to the lateral walls of the channel, which we assume oriented along the x direction. A pressure-driven flow, entraining a mixture of suspended objects of different size, is forced through the lattice. Because of the small size of the suspended objects and of the prevailing laminar flow conditions, particle inertia can safely be neglected in most of the cases thus implying a linear relationship between deterministic drive and instantaneous particle velocity Maxey and Riley (1983). In this overdamped regime, the microdynamical equation governing the local motion of a supposedly spherical particle reduces to a Langevin-type stochastic differential equation, which, in dimensionless form, writes

$$d\mathbf{x} = -\mathbf{v}(\mathbf{x}) dt + \sqrt{2/\text{Pe}} d\boldsymbol{\xi}, \quad (20)$$

where \mathbf{x} is the instantaneous position of the center of the particle, $\mathbf{v}(\mathbf{x})$ represents the deterministic drive, $d\boldsymbol{\xi}$ is a vector-valued Wiener process characterized by zero mean and unit variance, and where $\text{Pe} = U\ell/\mathcal{D}$ is the particle Peclet number, U , ℓ , and \mathcal{D} being a characteristic velocity, a characteristic length, and the particle bare diffusivity, respectively. In what follows U is set equal to the average velocity of the carrier flow, whereas the edge of the elementary cell of the periodic lattice (see the grey shaded box of Fig. 3a) is assumed as characteristic length ℓ . Note

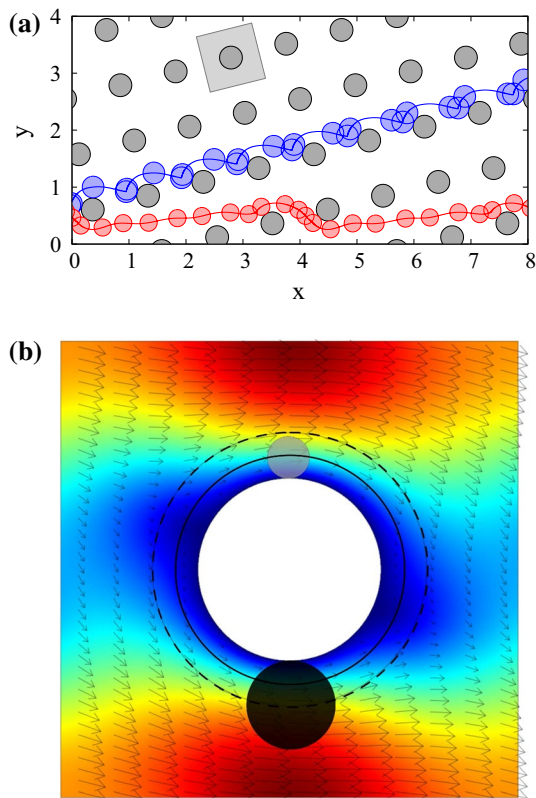


Fig. 3 a Lattice geometry and kinematic trajectories of finite-sized particles showed in their actual relative size (see main text for details). The *gray-shaded box* depicts the unit periodic cell. The average velocity of the carrier flow is oriented along the *x* axis. The lattice is slanted by an angle $\theta_l = \tan(1/4)$ w.r.t. the *x*-axis. The smaller particle (*red*) undergoes a zig-zag motion along *x*. The bigger particle (*blue*) follows a displaced mode along the lattice direction. **b** Structure of the pressure-driven periodic Stokes flow in the unit cell domain. The *contour plot* depicts the magnitude of the (dimensionless) velocity of the carrier flow, ranging from zero (*intense blue*) near the obstacle walls, to 2.5 (*intense red*) at the center of the restricted cross-section between adjacent obstacles. The *white area* depicts the physical obstacle. The *thick continuous* and *broken lines* depict the size of the effective obstacles for each of the particle sizes shown

that the deterministic drive $\mathbf{v}(\mathbf{x})$ results as the superposition of two separate contributions, namely the Stokesian drag acted upon the particle by the surrounding fluid, and the action of the impermeable obstacles, which forces the (center of the) particles to deviate from a purely advective motion, where the particle would passively trace the flow streamline through its center. The analysis of the specific particle-obstacle and particle-fluid interactions and its impact on separation performance has been object of intense theoretical, numerical and experimental research, both for fixed Frechette and Drazer (2009) and deformable Krüger et al. (2014) particle shapes. In what follows, we assume a recently proposed rigid-core model Cerbelli et al. (2013) for analyzing the impact of Brownian fluctuations

on particle transport. Briefly, this model assimilates the particle to a point-sized tracer collapsed at the particle center, which passively follows the unperturbed pressure-driven Stokes flow through the obstacle lattice, until its center comes to a distance equal to the particle radius from the boundary of an obstacle. At vanishing distance of the colliding surfaces, it is assumed that the particle-obstacle interaction is such as to annihilate the component of particle velocity normal to the obstacle surface, so that the particle glides around the obstacle under the action of the tangential velocity component, which is assumed unperturbed. In the case of cylindrical obstacles and rigid spherical particles, the overall action of the deterministic drive is therefore concisely represented by a passive point-sized tracer moving through a lattice of *effective obstacles* whose radius is equal to the radius of the physical obstacle plus the particle radius. It is worth observing that this simplified approach overlooks specific phenomena that may prove important in defining the deterministic component of particle motion. In this respect, the shape variation of the suspended object due to fluid-particle or to obstacle-particle interactions Krüger et al. (2014), Benke et al. (2011, 2013) is apt to be a crucial one.

Figure 3b shows the structure of the unperturbed steady Stokes flow within the elementary periodicity cell obtained through a finite-element solver by discretizing the domain in order 10^5 triangular element. The discretized solution is then bilinearly interpolated in order to define the drag component of the deterministic drive $\mathbf{v}(\mathbf{x})$ entering Eq. (20). In the same figure panel, the particle transport domain defined by the effective obstacle is also depicted for different particle sizes. The implementation of the effective obstacle model to practically relevant operating conditions and feasible device geometries has been recently analyzed in some detail Cerbelli et al. (2013), Cerbelli (2012). This analysis suggests that the large-scale structure of particle transport is indeed consistent with the effective transport template expressed by Eq. (1). Specifically, results stemming from ensemble statistics of Eq. (20) indicate that (i) both the average particle velocity \mathbf{W} , and the effective dispersion tensor \mathbb{D} depend sensitively on operating conditions (e.g. flowrate) and particle size (ii) large-scale dispersion is typically enhanced over the bare particle diffusivity and is generally strongly anisotropic (iii) the principal axes of \mathbb{D} are slanted with respect to both the average direction of the carrier flow and the average particle velocity \mathbf{W} . This having been established in previous work, we here proceed to investigate the relevance of the steady-state template discussed in the first part of this article to a realistic continuous fractionation process exploiting deterministic lateral displacement.

As a case study, we consider the geometry depicted in Fig. 3a, which is defined by a lattice angle $\theta_l = \tan(1/4)$,

and a post radius equal to 0.2 (all lengths are henceforth scaled to the edge of the unit periodicity cell). Particles of dimensionless radii ρ_p in the range $0.15 \leq \rho_p \leq 0.2$ are next considered. Figure 3a shows the trajectories of the center of the particles (continuous thick lines) superimposed to instantaneous snapshots of the particles shown in their actual relative size at regular intervals of time for $\rho_p = 0.15$ and $\rho_p = 0.20$ in the absence of diffusion (purely kinematic motion, $1/Pe \rightarrow 0$). One observes that the results of the effective obstacle model are consistent with the qualitative picture of the separation mechanism proposed in Refs Huang et al. (2004), Inglis et al. (2006). Bearing in mind this kinematic picture, the obvious question is to determine how the presence of Brownian fluctuations in Eq. (20) modifies the individual particle trajectories and how the dispersion bandwidth depicted in the schematic drawing of Fig. 1 is affected by particle size and by the flowrate (quantified by the the particle Pe parameter). To address these questions, we use Eq. 20 to generate a large number (order 10^5) of noise-driven trajectories all originating at a fixed location (assumed as the origin of the coordinate system) for each particle size, and we record the y value of the first intersection of each trajectory with a device cross section at \bar{x} , where \bar{x} denotes the dimensionless distance from the source feed downstream the channel axis x . Figure 4 shows the behavior of few individual particles trajectories for particle sizes $\rho_A = 0.15$ and $\rho_B = 0.2$ for $Pe = Pe_A = 10^3$. In this computations, the value of Pe_B is set to $Pe_B = Pe_A \rho_B / \rho_A$ to account for the fact that the particles are dragged by the same carrier flow, consistently with the Stokes-Einstein equation for the estimate of the bare particle diffusivity. Henceforth, we use the plain symbol Pe to denote $Pe(\rho_A)$, with the understanding that

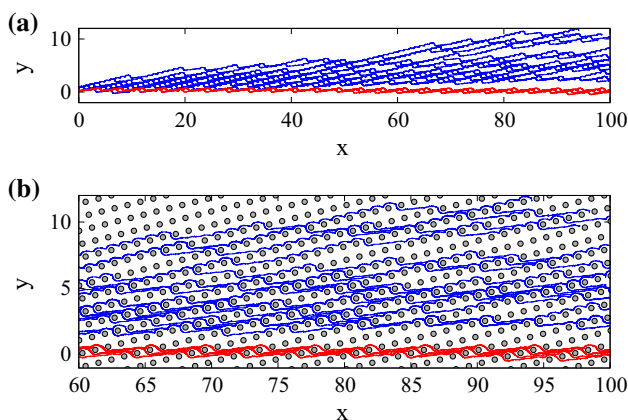


Fig. 4 Noisy trajectories of suspended particles at $Pe = 10^3$ (see main text for details). **a** Blue (dark grey) and red (light grey) lines depict the trajectories of the center of individual particle paths for $\rho_A = 0.2$ and $\rho_A = 0.15$, respectively. **b** Zoom-in showing the size of the physical obstacles

that the Pe number for particles of size different from ρ_A in Eq. (20) is scaled according to the radii ratio.

Note that the size of the larger particle was chosen close to the critical value separating the two transport modes depicted in Fig. 3a. The extent of the current broadening due to spanwise dispersion (i.e. in the y direction) is strikingly dependent on particle size. The dependence is altogether counter-intuitive, meaning that bigger particles—therefore characterized by a larger Pe value—are by far dispersed more pronouncedly than smaller ones. It is worth observing that this theoretical prediction is confirmed by recent experiments in gravity-driven deterministic lateral displacement devices Devendra and Drazer (2012).

We observe that in practical implementations of the separation method, particles cross thousands of unit cells before they are collected at the device exit, and therefore \bar{x} is of order 10^3 or larger, thus suggesting that the approximate solution expressed by Eq. (16) might be appropriate to describe the transport process.

From the y -values of the first intersections of individual particle paths with a fixed cross-section at \bar{x} , one can construct the discretized counterpart of the normalized profiles $\Phi_v(\bar{x}, y)$ in Eq. (11) as the fraction of intersection falling between y and $y + \Delta y$. Specifically, when a large number of trajectories (order 10^5) are considered, the statistics of the first intersections of particle paths (regardless of the time required for the particle to get at the assigned cross-section) becomes time-independent (not shown for brevity) and proportional to the steady-state concentration field $\Phi_v(\bar{x}, y)$. In agreement with the macroscopic character of the effective transport template, the bin size Δy is chosen of the order of one cell length, so as to smoothen out small-scale fluctuations of the particle concentration

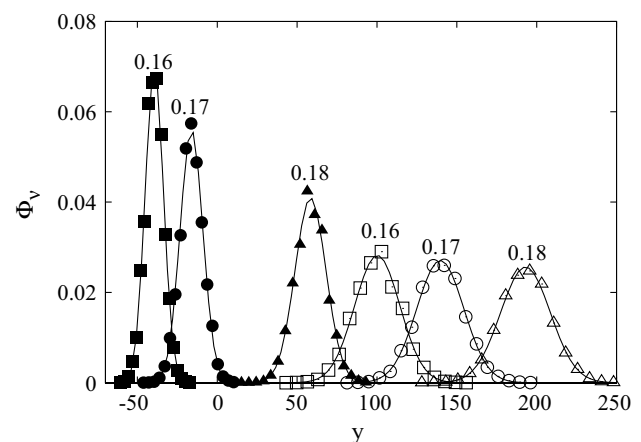


Fig. 5 Normalized distribution of the crossing y -coordinate at an outlet cross-section located at $\bar{x} = 3.9 \times 10^3$ downstream the feed source for particles of different sizes, $\rho = 0.16$; 0.17 ; 0.18 . Empty and filled symbols are associated with $Pe = 10^2$ and $Pe = 10^3$, respectively

profile. Figure 5 shows the Probability Density Function (henceforth PDF) of the intersections for three dimensionless particle sizes, $\rho_p = 0.16; 0.17; 0.18$ at different values of the Pe parameter, namely $Pe = 10^2$ (solid symbols) and $Pe = 10^3$ (empty symbols).

As can be observed, the average exit position of particle paths (approximately identified by the peak of the distribution) is extremely sensitive to value of the Pe parameter, whereas the dispersion width is less sensitive to variation of Pe, especially for the largest particle size $\rho_p = 0.18$. It is worth highlighting that the results depicted in Fig. 4 are qualitatively consistent with the experimental determination of particle concentration profiles in pressure-driven DLD devices Huang et al. (2004), as regards both the behavior of the profile peak and the dispersion bandwidth.

One notes that the profiles at the larger Pe value indicate that an efficient separation of the larger sized particles ($\rho_p = 0.18$) is possible at these operating conditions, a possibility that is not predicted by the purely kinematic model, since all of the particle sizes shown are below the critical value separating the zig-zag and displaced modes in the $Pe \rightarrow \infty$ limit, and should therefore display no average deflection with respect to the direction of the drive. This means that Brownian diffusion causes two oppositely directed effects on separation, namely (i) a sensitive dependence of the average deflection angle that makes the fractionation of a multidispersed mixture possible even in cases where purely kinematic models do not predict any separation, and (ii) a current-broadening effect caused by dispersion-enhanced regimes that hinders separation. Far enough from the feed source, i.e. at \bar{x} of order 10^2 or more,

the first (separation-enhancing) effect depends linearly upon the distance \bar{x} in that the profile peak is aligned with the effective particle velocity for each given particle size. Figure 6 shows the behavior of the average and the variance of the crossing y-coordinate associated with the first intersection of noisy particle trajectories with a generic device cross-section located at dimensionless distance \bar{x} downstream the particle feed.

Besides, as predicted by Eq. 14, the dispersion-enhancing (i.e. separation-hindering) effect, quantified by the variance $\sigma(\bar{x})$ of the normalized particle concentration profiles, scales as $\sqrt{2D_{\text{eff}}\bar{x}}$. Figure 7a provides an illustration of this behavior for $\rho_p = 0.15$ at Pe values ranging from 10^2 to 5×10^3 , where it is evident that the \bar{x} -asymptotic scaling is already well established at $\bar{x} \geq 10^2$. By reason of the above observation, from Eq. (13) one gathers that particles of different type can always be resolved if the device length is large enough, in that the ratio the r.h.s. of Eq. (13) globally grows as $\sqrt{\bar{x}}$. Clearly, this theoretical argument does not consider practical aspects of the separation such as exceedingly large values of the pressure drop required (which can ultimately result in mechanical breakdown of the separation equipment), nor it takes into account the larger transient needed to reach steady-state conditions.

From data such as those depicted in Fig. 7a, the dependence of the continuous dispersion coefficient D_{eff} on the (dimensionless) bare particle diffusivity $1/Pe$ can be computed for each particle size. The results of this computation are shown in Fig. 7b for $\rho_p = 0.15$ (triangles), $\rho_p = 0.18$ (squares), and $\rho_p = 0.19$ (circles). The dimensionless bare particle diffusivity $1/Pe$ is also depicted in the same figure (continuous line), so that an immediate visualization of the dispersion enhancement due to the interaction between deterministic and Brownian motion at microscales can be appreciated. The smaller particle size is characterized by a very modest dispersion enhancement. An effective enhanced-dispersion regime is instead evident for $\rho_p = 0.18$, where $D_{\text{eff}} \simeq 1/\sqrt{Pe}$, as depicted by the dashed line in the figure panel. Finally, a singular dispersion-enhanced regime characterizes the larger particle size $\rho_p = 0.19$ which is very close to the critical size, say ρ_c , predicted by the kinematic model, which, for this lattice geometry, falls in the interval $0.1875 < \rho_c < 0.19$ [see Ref Cerbelli et al. (2013)]. As pointed out above, the occurrence of critical dispersion regimes near critical particle sizes has been both experimentally observed in continuous fractionation process Devendra and Drazer (2012), and theoretically justified in simplified models of transport through periodic lattice of potentials Cerbelli (2013). From the data depicted in Fig. 7a associated with the particle size $\rho_p = 0.19$, one gathers that at practically relevant values of the Pe parameter (e.g. a 1 μm bacterium in the experimental conditions used to test the device proposed in Ref. Huang et al. (2004) is characterized by a Pe value of order 5×10^3), the dispersion enhancement

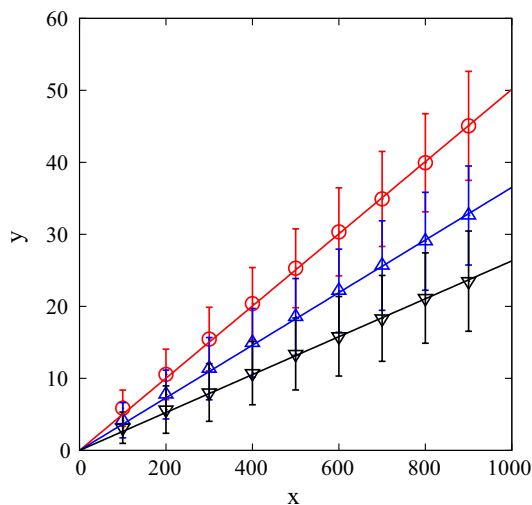


Fig. 6 Average crossing coordinate versus \bar{x} for different particle size at $Pe = 10^2$. (Black)-triangles $\rho_p = 0.16$; (blue)-Delta symbols $\rho_p = 0.17$; (red)-circles $\rho_p = 0.18$. The errorbar depict the magnitude of the profile variance $\sigma(\bar{x})$. The straight lines depict the best fit of the average crossing coordinate in the interval $5 \times 10^2 \leq \bar{x} \leq 10^3$

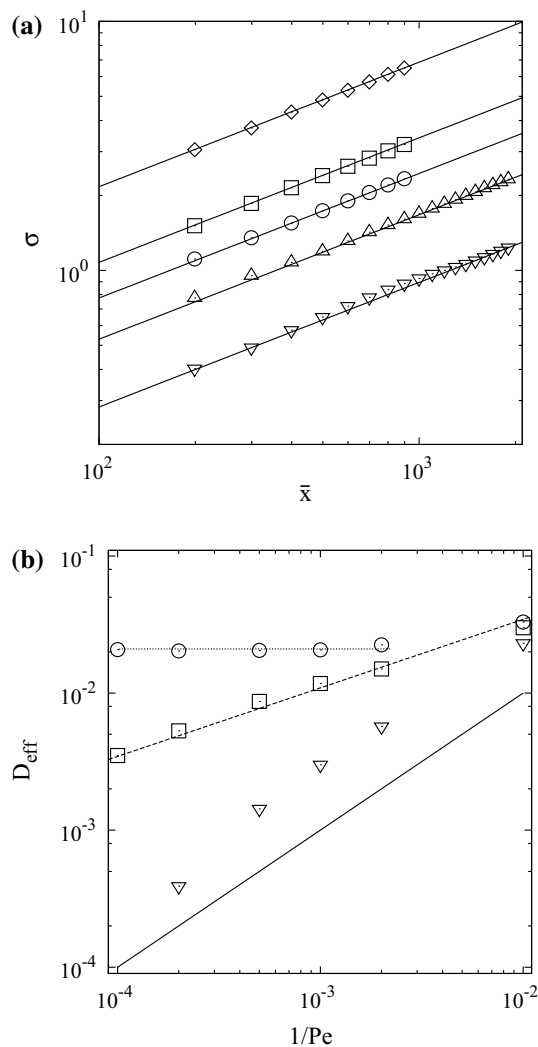


Fig. 7 **a** Variance $\sigma(\bar{x})$ of the normalized particle concentration profiles versus the dimensionless distance \bar{x} from the feed source downstream the average direction of the carrier flow for the particle radius $\rho_p = 0.15$; *Diamond* : $Pe = 10^2$; *square* : $Pe = 5 \times 10^2$; *circle* : $Pe = 10^3$; *triangle* : $Pe = 2 \times 10^3$; *inverted triangle* : $Pe = 5 \times 10^3$. The *continuous line* represent the scaling $\sigma(\bar{x}) = \sqrt{2D_{\text{eff}}\bar{x}}$, where D_{eff} is regarded as a fitting parameter. **b** Effective dispersion coefficient versus $1/Pe$; *inverted triangle* : $\rho_p = 0.15$; *square* : $\rho_p = 0.18$; *circle* : $\rho_p = 0.19$. The *continuous line* represents the dimensionless bare particle diffusivity $1/Pe$, the *dashed line* depicts the scaling $D_{\text{eff}} \simeq \text{Const.}/\sqrt{Pe}$

factor over the bare particle diffusivity can exceed two orders of magnitude, which implies an error of more than a tenfold factor in the estimate of the steady-state profile variance.

5 Conclusions

We propose an effective transport template for characterizing continuous fractionation processes of suspended mesoscopic objects in periodically-patterned microfluidic

devices in the presence of diffusion. Assuming a general form of the transport equation, characterized by a constant effective velocity \mathbf{W} and a spatially homogeneous, yet non-isotropic, effective dispersion tensor \mathbb{D} , we derive in closed-form the steady-state solution associated with a localized particle feed, useful for the interpretation of steady-state measurements of particle concentration profiles (e.g. obtained through long-exposure micrography of fluorescent particles). At large (dimensionless) distance \bar{x} from the feed source along the average direction of the deterministic drive, the cross-sectional concentration profiles attain an almost Gaussian structure, with a peak position that depends linearly on \bar{x} through the effective velocity parameters, and a profile variance that scales as $\sigma(\bar{x}) = \sqrt{2D_{\text{eff}}\bar{x}}$, where the continuous dispersion coefficient, D_{eff} , is primarily controlled by the projection of the effective dispersion tensor along the direction orthogonal to \mathbf{W} . To illustrate the occurrence of effective transport in microfluidic separation processes, we use numerical results stemming from a recently proposed model for predicting size-based particle separation in Deterministic Lateral Displacement Devices. These results suggest that dispersion-enhanced regimes arise as a consequence of the microscale interaction between the deterministic drive (presently constituted by the Stokesian drag of the carrier flow) and Brownian diffusion. The extent of dispersion enhancement is strongly affected by particle size. Specifically, particles whose dimension is close to the critical size separating zig-zag and displaced modes (as predicted by a purely kinematic template) show a giant enhancement of dispersion. At values of the particle Peclet number that are commonly found in concrete applications of DLD separations, this giant enhancement can yield values of the dispersion bandwidth that are an order of magnitude larger with respect to what can be predicted based on the bare particle diffusivity. This suggests that an accurate prediction of separation resolution in continuous particle fractionation cannot do away with an accurate modeling of the intertwined action between deterministic motion and Brownian fluctuations at the microscale.

Appendix

In what follows, we prove the relationship

$$D_{\text{eff}} = \frac{D_1 \sin^2 \Theta'_{\mathbf{W}} + D_2 \cos^2 \Theta'_{\mathbf{W}}}{|\cos^3(\Theta'_{\mathbf{W}} + \Theta_D)|} = \frac{D_{\perp}}{|\cos^3 \Theta_{\mathbf{W}}|}, \quad (21)$$

expressed by Eq. (14) in the main article. Figure 8 depicts the global coordinate axes together with the $\xi_1 \xi_2$ coordinate system that is collinear with the principal axes of the effective diffusion tensor \mathbb{D} .

With reference to this figure, consider the asymptotic approximation to the steady-state particle concentration field expressed by Eq. (13) of the main article, which we report below

$$C_\infty(\xi_1, \xi_2) \simeq \frac{A}{\sqrt{\pi}} \frac{\exp\{\beta(\xi_1, \xi_2) - h(\xi_1, \xi_2)\}}{\sqrt{h(\xi_1, \xi_2)}}, \tag{22}$$

Our approach to prove the result in Eq. (21) is to determine the structure of the one-dimensional cross-sectional profile $C_\infty(\xi_1(u), \xi_2(u))$ where u is a local coordinate system with origin at the point $\bar{P} = (\bar{x}, \tan(\Theta'_w + \Theta_D)\bar{x})$ at the intersection between the straight line r and the cross-section at \bar{x} [compare Fig. S8 and Fig. 1 of the main article]. As a first observation, note that the argument, say $g(\xi_1, \xi_2)$,

$$g(\xi_1, \xi_2) = \beta(\xi_1, \xi_2) - h(\xi_1, \xi_2), \tag{23}$$

of the exponential function at the r.h.s of Eq. (22) vanishes identically onto the r -line, together with its first ξ_1 - and ξ_2 -derivatives, $\partial_{\xi_1}g$, and $\partial_{\xi_2}g$. Thus, if one expands in Taylor series $G(u) = g(\xi_1(u), \xi_2(u))$ as a function of u about the point \bar{P} one gets

$$\begin{aligned} G(u) &= G(0) + G'(u)|_0 u + \frac{1}{2} G''(u)|_0 u^2 + o(u^3) \\ &= \frac{1}{2} G''(u)|_0 u^2 \end{aligned} \tag{24}$$

Since $u = 0$ corresponds to the point \bar{P} one gets that $G(0) = 0$, and $G'(u)|_0 = \nabla g \cdot \mathbf{e}_u = \mathbf{0} \cdot \mathbf{e}_u = 0$, where $\nabla = (\partial_{\xi_1}, \partial_{\xi_2})$ and where \mathbf{e}_u is a unit vector parallel the cross-section. Therefore one obtains that onto the device cross-section the one-dimensional concentration profile can be approximated as

$$C_\infty(\xi_1(u), \xi_2(u)) \simeq \frac{A}{\sqrt{\pi h(\xi_1(u), \xi_2(u))}} \exp\left\{\frac{G''(u)|_0 u^2}{2}\right\} \tag{25}$$

It can be observed that at large \bar{x} values, the denominator at the r.h.s. of Eq. (25) is nearly constant in the range where the exponential factor is significantly different from zero. This implies, that, within this approximation, the

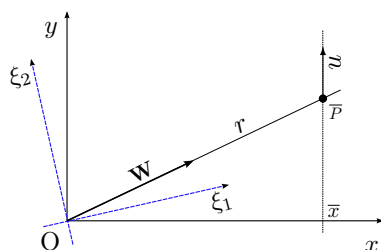


Fig. 8 Global versus intrinsic coordinate system

one-dimensional profile in Eq. (25) possesses a Gaussian structure, with a variance σ given by

$$\sigma^2 = -\frac{1}{G''(u)|_0} \tag{26}$$

Therefore, the profile variance σ at \bar{x} can be estimated from the second derivative of the the function $G(u)$ at $u = 0$, which corresponds to \bar{P} . One obtains

$$\begin{aligned} G''(u)|_0 &= \frac{\partial^2 g}{\partial \xi_1^2} \left(\frac{d\xi_1}{du}\right)^2 + \frac{\partial^2 g}{\partial \xi_2^2} \left(\frac{d\xi_2}{du}\right)^2 \\ &+ 2 \frac{\partial^2 g}{\partial \xi_1 \partial \xi_2} \left(\frac{d\xi_1}{du}\right) \left(\frac{d\xi_2}{du}\right) \end{aligned} \tag{27}$$

Note that since $\beta(\xi_1, \xi_2)$ in Eq. (23) is a linear function of its arguments, only the second derivatives of $h(\xi_1, \xi_2)$ contribute to the partial derivatives of the g function in Eq. (27). The explicit computation of the derivatives at the r.h.s. of Eq. (27) yields, after simple algebraic manipulations,

$$\begin{aligned} G''(u)|_0 &= h''(u)|_0 = \frac{1}{2 D_{\perp \bar{x}}} |\cos(\Theta_w)| (\mathbf{e}_u \cdot \mathbf{e}_w)^2 \\ &= \frac{|\cos(\Theta_w)|^3}{2 D_{\perp \bar{x}}} \end{aligned} \tag{28}$$

where $D_{\perp} = D_1 \sin^2 \Theta'_w + D_2 \cos^2 \Theta'_w$, and where \mathbf{e}_w and \mathbf{e}_x are unit vectors parallel to \mathbf{W} and to the x axis, respectively. From Eq. (26) one obtains

$$\sigma^2 = 2 D_{\text{eff}} \bar{x} = \frac{2 D_{\perp \bar{x}}}{|\cos(\Theta_w)|^3} \tag{29}$$

which is equivalent to Eq. (21).

References

Abramowitz M, Stegun IA (1972) Handbook of mathematical functions: with formulas, graphs, and mathematical tables. Courier Dover Publications, New York

Autebert J, Coudert B, Bidard F-C, Pierga J-Y, Descroix S, Malaquin L, Viovy J-L (2012) Microfluidic: an innovative tool for efficient cell sorting. *Methods* 57:297–307

Benke M, Shapiro E, Drikakis D (2011) Mechanical behaviour of DNA molecules-elasticity and migration. *Med Eng Phys* 33:883–886

Benke M, Shapiro E, Drikakis D (2013) On mesoscale modelling of dsDNA molecules in fluid flow. *J Comput Theor Nanosci* 10:697–704

Bogunovic L, Eichhorn R, Regtmeier J, Anselmetti D, Reimann P (2012) Particle sorting by a structured microfluidic ratchet device with tunable selectivity: theory and experiment. *Soft Matter* 8:3900–3907

Brenner H, Edwards D (1993) Macrotransport processes; Butterworth-Heinemann Series in Chemical Engineering

Bruus H (2012) Acoustofluidics 7: the acoustic radiation force on small particles. *Lab Chip* 12:1014–1021

- Cerbelli S (2013) Critical dispersion of advecting-diffusing tracers in periodic landscapes of hard-wall symmetric potentials. *Phys Rev E* 87(6):060102
- Cerbelli S (2012) Separation of polydisperse particle mixtures by deterministic lateral displacement. The impact of particle diffusivity on separation efficiency. *Asia Pac J Chem Eng* 7:S356–S371
- Chen S (2013) Driven transport of particles in 3D ordered porous media. *J Chem Phys* 139(7):074904
- Collins D, Alan T, Neild A (2014) Particle separation using virtual deterministic lateral displacement (vDLD). *Lab Chip* 14:1595–1603
- Cerbelli S, Giona M, Garofalo F (2013) Quantifying dispersion of finite-sized particles in deterministic lateral displacement microflow separators through Brenner's macrotransport paradigm. *Microfluid Nanofluid* 15:431–449
- Devendra R, Drazer G (2012) Gravity driven deterministic lateral displacement for particle separation in microfluidic devices. *Anal Chem* 84:10621–10627
- Dorfman K, King S, Olson D, Thomas J, Tree D (2013) Beyond gel electrophoresis: microfluidic separations, fluorescence burst analysis, and DNA stretching. *Chem Rev* 113:2584–2667
- Frechette J, Drazer G (2009) Directional locking and deterministic separation in periodic arrays. *J Fluid Mech* 627:379–401
- Ghosh P, Hnggi P, Marchesoni F, Martens S, Nori F, Schimansky-Geier L, Schmid G (2012) Driven Brownian transport through arrays of symmetric obstacles. *Phys Rev E* 85:011101
- Giddings JC (1991) Unified separation science. Wiley, New York
- Gleeson J, Sancho J, Lacasta A, Lindenberg K (2006) Analytical approach to sorting in periodic and random potentials. *Phys Rev E* 73:041102
- Gradshteyn I, Ryzhik I (2007) Table of integrals, series, and products. Academic Press, San Diego
- Green J, Radisic M, Murthy S (2009) Deterministic lateral displacement as a means to enrich large cells for tissue engineering. *Anal Chem* 81:9178–9182
- Gross M, Krüger T, Varnik F (2014) Fluctuations and diffusion in sheared athermal suspensions of deformable particles. *EPL (Europhysics Letters)* 108:68006
- Han K-H, Frazier A (2008) Lateral-driven continuous dielectrophoretic microseparators for blood cells suspended in a highly conductive medium. *Lab Chip* 8:1079–1086
- He K, Babaye Khorasani F, Retterer S, Thomas D, Conrad J, Krishnamoorti R (2013) Diffusive dynamics of nanoparticles in arrays of nanoposts. *ACS Nano* 7:5122–5130
- He K, Retterer S, Srijanto B, Conrad J, Krishnamoorti R (2014) Transport and dispersion of nanoparticles in periodic nanopost arrays. *ACS Nano* 8:4221–4227
- Heller M, Bruus H (2008) A theoretical analysis of the resolution due to diffusion and size dispersion of particles in deterministic lateral displacement devices. *J Micromech Microeng* 18:075030
- Hnggi P, Marchesoni F (2009) Artificial Brownian motors: controlling transport on the nanoscale. *Rev Mod Phys* 81:387–442
- Huang L, Cox E, Austin R, Sturm J (2003) Tilted Brownian ratchet for DNA analysis. *Anal Chem* 75:6963–6967
- Huang L, Cox E, Austin R, Sturm J (2004) Continuous particle separation through deterministic lateral displacement. *Science* 304:987–990
- Inglis D (2009) Efficient microfluidic particle separation arrays. *Appl Phys Lett* 94(1):013510
- Inglis D, Davis J, Austin R, Sturm J (2006) Critical particle size for fractionation by deterministic lateral displacement. *Lab Chip* 6:655–658
- Inglis D, Davis J, Zieziulewicz T, Lawrence D, Austin R, Sturm J (2008) Determining blood cell size using microfluidic hydrodynamics. *J Immunol Methods* 329:151–156
- Jain A, Posner J (2008) Particle dispersion and separation resolution of pinched flow fractionation. *Anal Chem* 80:1641–1648
- Jonas A, Zemanek P (2008) Light at work: the use of optical forces for particle manipulation, sorting, and analysis. *Electrophoresis* 29:4813–4851
- Kirchner J, Hasselbrink E, Jr (2005) Dispersion of solute by electrokinetic flow through post arrays and wavy-walled channels. *Anal Chem* 77:1140–1146
- Kralj J, Lis M, Schmidt M, Jensen K (2006) Continuous dielectrophoretic size-based particle sorting. *Anal Chem* 78:5019–5025
- Krüger T, Holmes D, Coveney P (2014) Deformability-based red blood cell separation in deterministic lateral displacement devices: a simulation study. *Biomicrofluidics* 8(5):054114
- Kulrattanarak T, van der Sman R, Schroëen C, Boom R (2008) Classification and evaluation of microfluidic devices for continuous suspension fractionation. *Adv Colloid Interface Sci* 142:53–66
- Lenhoff A, Laurell T (2010) Continuous separation of cells and particles in microfluidic systems. *Chem Soc Rev* 39:1203–1217
- Ling S, Lam Y, Chian K (2012) Continuous cell separation using dielectrophoresis through asymmetric and periodic microelectrode array. *Anal Chem* 84:6463–6470
- Long B, Heller M, Beech J, Linke H, Bruus H, Tegenfeldt J (2008) Multidirectional sorting modes in deterministic lateral displacement devices. *Phys Rev E* 78:046304
- Loutherback K, Chou K, Newman J, Puchalla J, Austin R, Sturm J (2010) Improved performance of deterministic lateral displacement arrays with triangular posts. *Microfluid Nanofluid* 9:1143–1149
- Loutherback K, Puchalla J, Austin R, Sturm J (2009) Deterministic microfluidic ratchet. *Phys Rev Lett* 102:045301
- MacDonald M, Spalding G, Dholakia K (2003) Microfluidic sorting in an optical lattice. *Nature* 426:421–424
- Maxey M, Riley J (1983) Equation of motion for a small rigid sphere in a nonuniform flow. *Phys Fluids* 26:883–889
- Polyanin A, Manzhirov A (2007) Handbook of mathematics for scientists and engineers. Chapman & Hall/CRC, Boca Raton, FL
- Raynal F, Beuf A, Carrière P (2013) Numerical modeling of DNA-chip hybridization with chaotic advection. *Biomicrofluidics*, 7(3):034107
- Sia S, Whitesides G (2003) Microfluidic devices fabricated in poly(dimethylsiloxane) for biological studies. *Electrophoresis* 24:3563–3576
- Speer D, Eichhorn R, Reimann P (2012) Anisotropic diffusion in square lattice potentials: giant enhancement and control. *EPL* 97:60004
- Zhang C, Khoshmanesh K, Mitchell A, Kalantar-Zadeh K (2010) Dielectrophoresis for manipulation of micro/nano particles in microfluidic systems. *Anal Bioanal Chem* 396:401–420